Fermilab HINS Proton Ion Source Beam Studies

G. Apollinari, S. Chaurize, B. Hanna, G. Romanov, V. Scarpine, C. Schmidt
W-M Tam, J. Walton, R. Webber, V. Yakovlev, D. Zhang

November 15, 2009

The HINS proton ion source and low energy beam transport (LEBT) was successfully commissioned. It is capable to produce a 50 keV, 3 msec pulsed beam with a peak current greater than 20 mA (less than 50% proton, discussed below) at 2.5 Hz (0.7% duty factor). The beam is transported to the radio frequency quadrupole (RFQ) by the LEBT that consists of two focusing solenoids and four steering dipole magnets. To understand beam transmission through the RFQ, it is important to characterize the proton beam before connecting the LEBT to the RFQ. A wire scanner and a Faraday cup are temporarily installed at the exit of the LEBT to study the beam parameters. A schemetic drawing is shown in Fig. 1.

All data were taken using the wire scanner. We started with interpreting the signal measured by the wire scanner. Then, we performed a beam-base calibration to the steering dipole magnets. We then studied transverse motion coupling due to solenoidal field by measuring beam rotation through solenoid. Finally, together with a slit the wire scanner will form an emittance probe (slit-wire scanner assembly) for direct emittance measurement. Result from direct emittance measurement is compared to indirect measurement using solenoid variation method. Note that, due to high voltage supplies limitation in the early stage of operation, some of the measurements were made for beam below 50 keV. Unless specified, the beam energy is assumed to be 50 keV.

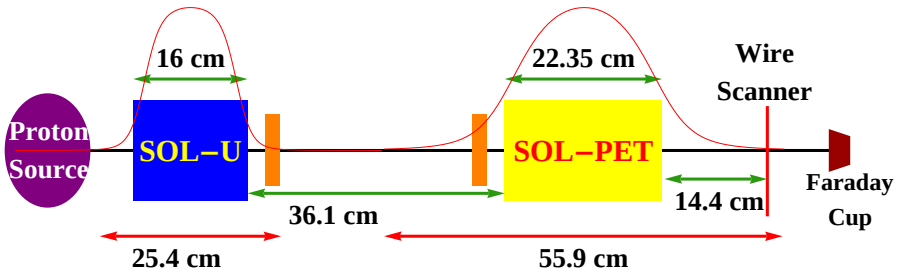

Figure 1: Layout of LEBT.

1 Transverse Beam Profile Measurement

Horizontal and vertical beam profiles are measured using the wire scanner. Fig. 2 shows the results of a vertical beam profile measurement for a 48 keV proton beam with a pulse length of 100 μs at a repetition rate of 0.5 Hz. The two solenoids were optimized to locate the beam waist at the wire scanner. The data points reflect the integrated electric charge as seen by the wire at every step across the beam pipe. The narrow peak is the profile of the proton beam. The background signal comes from other particle species (mainly H_2^+) being extracted from the source.

As shown in the figure, the background has an integrated signal that is larger than that of the proton. In fact, a peak current of 8 mA is recorded by the current transformer while the reading at the Faraday cup is only 3.5 mA, suggesting a beam loss of more than 50 %. In contrast, the results coming from TRACK simulation shows zero beam loss under the same solenoid settings. This suggests that more than 50 % of the beam is composed of non-proton ion species and that contribute to most of detected beam loss.

The possibility that the faster proton being separated from the slower H_2^+ is excluded. Consider a total length of 1 meter from the ion source to the wire scanner. Proton is half the weight of H_2^+ therefore at the same kinetic energy proton moves faster by a factor of $\sqrt{2}$. Suppose proton and H_2^+ leave the ion source at the same time. After 1 meter of travel, their time separation is about 0.134 μs, which is much smaller than the pulse length of 100 μs. So, at the wire scanner proton and H_2^+ are approximately at the same phase.

To extract the profile of the proton beam from the combined signal, two Gaussian distributions, one for the proton and one for the H_2^+, are used to fit the raw data. The expression used for fitting is

$$signal(x) = g(A_1, \sigma_1, x_{01}; x) + g(A_2, \sigma_2, x_{02}; x) \cdot pipe(x) + k, \tag{1}$$

where

$$g(A, \sigma, x_0, x) = A \cdot \exp(\frac{-(x - x_0)^2}{2\sigma^2}), \tag{2}$$

$$pipe(x) = \frac{1}{r}\sqrt{r^2 - x^2}, \tag{3}$$

where r is the radius of the beam pipe and k is a constant. The normalization factor, $pipe(x)$, is applied to the second Gaussian since, as shown in Fig. 2, the H_2^+ ions fill out the whole beam pipe, whose radius, r, is 17 mm.

The fitting has a coefficient of determination, the R^2 value, larger than 0.99 (see Fig. 2(a)). The profile of the proton beam is nicely extracted from the fitting (see Fig. 2(b)). The RMS beam size, σ_{rms}, or σ_1 in Eq. (1), obtained from this measurement is 0.64 mm. This measurement has been repeated for ten times. The error for such a measurement is $\pm$ 2 %. Fig. 3 is a plot showing the time structure of the proton beam pulse. This 100 μs pulse beam has a flat-top of about 50 μs.

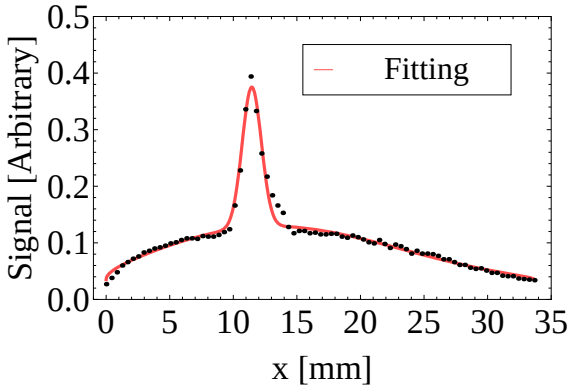

(a) Raw signal from the wire scanner. The red line is a double Gaussian fit. The fit has a R^2 value of greater than 0.99.

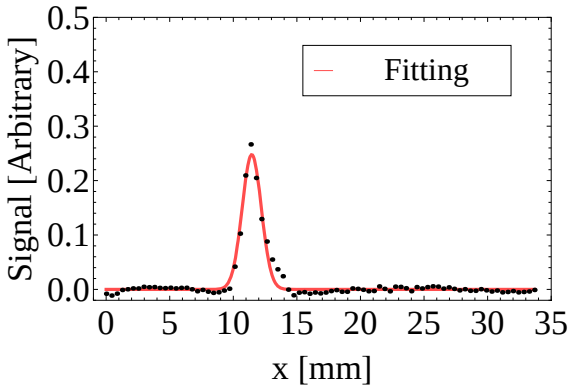

(b) The fit successfully extracts the profile of the proton beam from raw data.

Figure 2: Transverse beam profile measurement using wire scanner. Due to the presence of H_2^+ ions, two Gaussians are used to fit the data. The profile of the proton beam is nicely extracted from the raw data.

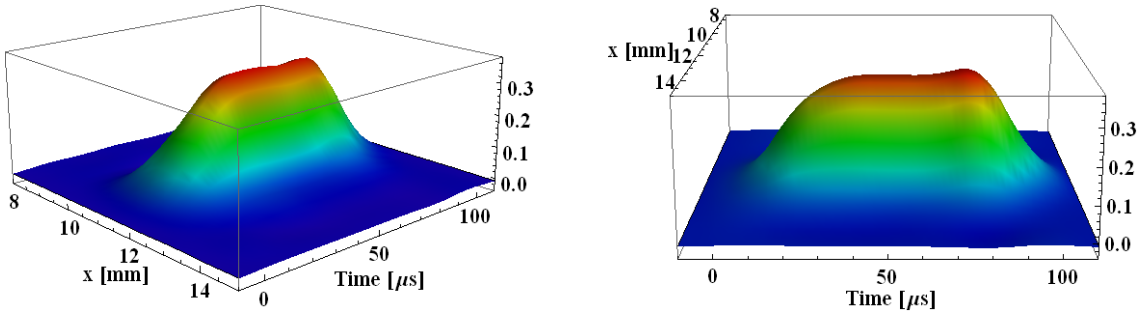

(a) (b)

Figure 3: The time structure of the beam pulse. This 100 μs beam pulse has a flat top of about 50 μs.

2 Beam Steering by the Dipole Magnets

In addition to beam profile measurement, the wire scanner can also be used to determine the position of the beam relative to the beam pipe. Beam deflection as a function of magnet strength is measured for a 45 keV proton beam.

In order to measure the beam deflection as a function the strength of the corrector dipole magnets, the downstream solenoid, SOL-D, is switched off to avoid x-y coupling. Fig. 4 shows the change in the beam profile (or position) as the strength of the dipoles is varied. Since the SOL-D is turned off, the size of the proton beam is much larger. Fortunately, the movement of the peak of the beam profile can still be clearly observed. The vertical position of the beam does not response to excitation in the horizontal dipole magnets (see Fig. 4(a) and 4(c)). Also, the horizontal position does not change with the strenght of vertical dipole magnets (see Fig. 4(b) and 4(d)). This suggests that the dipoles were well aligned such that x and y motion are not coupled up to our resolution. Note that the two horizontal dipoles bend the beam in different directions. This is also true for the two vertical dipoles.

The amount of beam deflection as a function of dipole strength can be estimated using the data plotted in Fig. 4. It can also be estimated by considering the angle of deflection of obtained from the Lorentz force law

$$\theta_d = \frac{e}{p}\int_{z_1}^{z_2} B dz = \frac{1}{B\rho}\int_{z_1}^{z_2} B dz \tag{4}$$

where e is the charge of an electron, $p = \gamma\beta mc$ is the momentum of the beam, and $B\rho = p/e$ is the momentum rigidity of the beam. B is the transverse magnetic field along the beam axis. For a proton beam at 45 keV the momentum rigidity is 30.653 kG-cm.

The estimated and measured spatial deflection of the beam at the wire scanner are plotted together in Fig. 5. For the downstream dipoles, result from calculation was 3.3 mm/Amp. Measurement result for DIP-DH was 3.1 mm/Amp and that for DIP-DV was 2.8 mm/Amp. However, the result for the upstream dipoles, DIP-UH and DIP-UV, shows

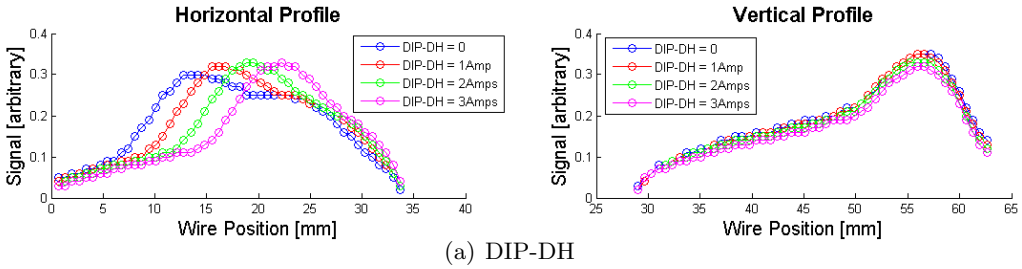

(a) DIP-DH

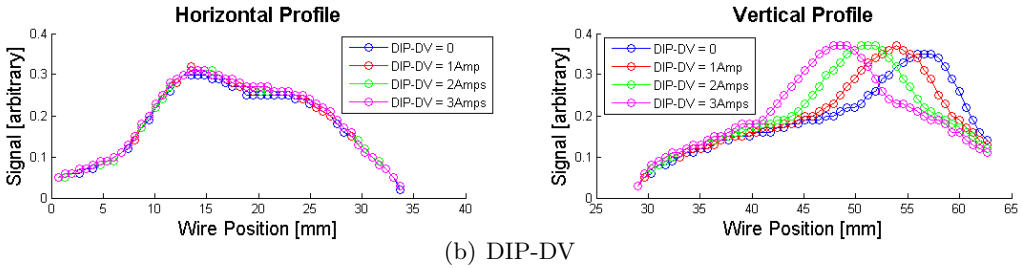

(b) DIP-DV

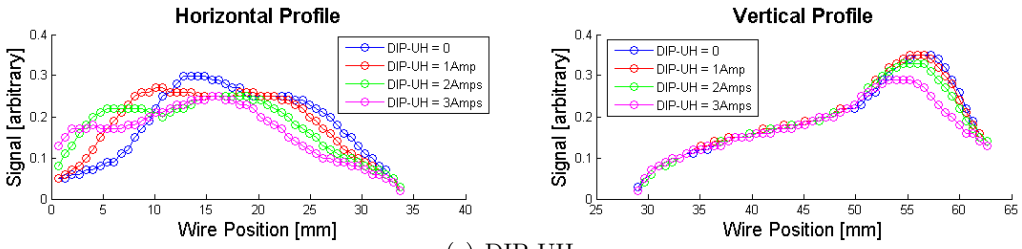

(c) DIP-UH

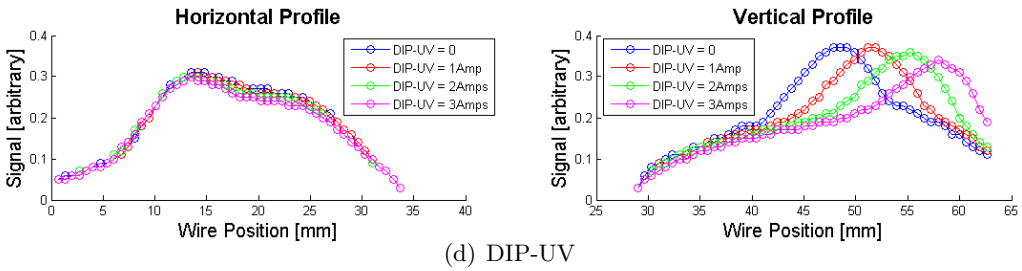

(d) DIP-UV

Figure 4: Beam profile measurement under different dipole strengths. The solenoid SOL-D is switched off to avoid x-y coupling.

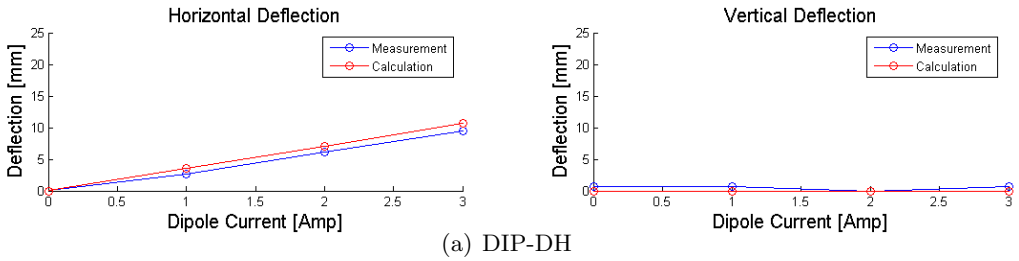

(a) DIP-DH

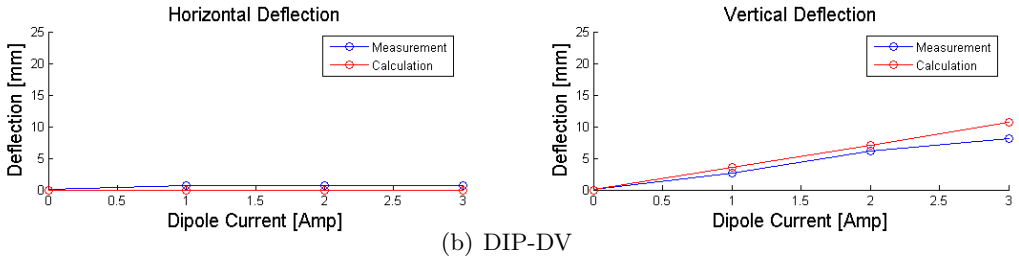

(b) DIP-DV

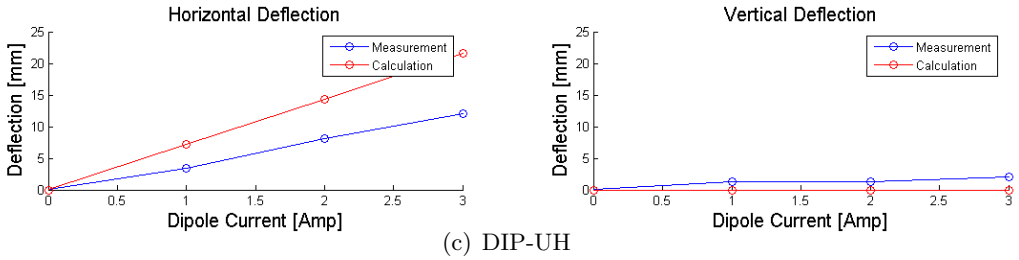

(c) DIP-UH

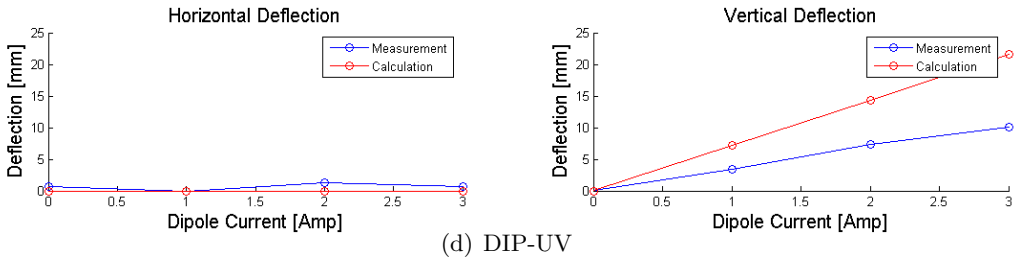

(d) DIP-UV

Figure 5: Beam spatial deflection at the location of the wire scanner. Comparison is made between measurement result shown in Fig. 4 and calculation using Eq. (4).

significantly smaller deflection compared to calculation. Result from calculation was 7.3 mm/Amp while measurement result for DIP-UH was 4.0 mm/Amp and that for DIP-UV was 3.5 mm/Amp. This is due to the fact that the two upstream dipoles are located too close to the upstream solenoid, SOL-U, such that the dipole field was "absorbed" into the iron shielding of the solenoid, which shortened span of the dipole field and lowered the field amplitude. Another implication from this result is that the alignment (roll angle) of the dipoles is acceptable up to the resolution of beam position measurement using the wire scanner. This step is crucial in the measurement of beam rotation due to solenoidal field, which is discussed in next section.

3 Beam Rotation by Focusing Solenoid

When a beam travels through a solenoid, its horizontal and vertical dynamics are coupled due to the beam rotation by the solenoidal field. In the following, we study beam rotation due to solenoidal field by (1) solenoid lens model and (2) particle tracking. Then we will show measurement results for beam rotation by the downstream solenoid SOL-PET. Results from analytical calculation and measurement will be compared.

3.1 Solenoid as a Lens

The treatment follows the discussion in [1]. We can model a solenoid as a lens by considering that the magnetic field is uniform inside the solenoid and zero otherwise. The solenoid has a length of L. Inside the solenoid, for $0 < z < L$, the magnetic field is uniform ($\vec{B} = B_0\hat{z}$). The magnetic field is zero outside the solenoid. For region near $z = 0$ and $z = L$, the field rises rapidly from zero to B_0 (or drops from B_0 to zero).

Inside the solenoid ($0 < z < L$), in a uniform solenoidal magnetic field, the trajectory of a charged particle is in general a helix. The projection of the helix on the x-y plane is a circle of radius R. From $\vec{F} = q(\vec{v} \times \vec{B})$, the radius of the circle, R, is given by

$$\frac{\gamma m v_\perp^2}{R} = q v_\perp B_0, \tag{5}$$

so that

$$R = \frac{\gamma m v_\perp}{q B_0}, \tag{6}$$

where γ is the relativistic Lorentz factor, m is the rest mass of the particle, q is the charge of the particle, and $v_\perp$ is the particle's velocity projected onto the x-y plane. The cyclotron frequency, ω, is given by

$$\omega = \frac{v_\perp}{R} = \frac{q B_0}{\gamma m}. \tag{7}$$

Using the cyclotron frequency, we can calculate the aximuthal angle, ϕ_h, rotated by the particle's trajectory about the axis of the helix. This is given by the product of the cyclotron

and the time it takes for the particle to traverse the field:

$$|\phi_h| = \omega t = \frac{qB_0}{\gamma m}\frac{L}{v_z} \approx \frac{qB_0 L}{p}, \tag{8}$$

where $p = \gamma\beta mc$ is the momentum of the particle, and $v_z \gg v_\perp$ is assumed.

Near the two ends of the solenoid, $z = 0$ and $z = L$, where the axial magnetic field is changing, Maxwell equation suggests that there exists a radial component of the magnetic field, given by

$$\nabla \cdot \vec{B} = \frac{1}{r}\frac{\partial(rB_r)}{\partial r} + \frac{\partial B_z}{\partial z} = 0, \tag{9}$$

so that

$$B_r \approx -\frac{r}{2}\frac{\partial B_z}{\partial z}. \tag{10}$$

This radial field component gives an azimuthal kick to the particle when it enters or exits the solenoid. The change in the azimuthal momentum can be obtained from the Lorentz force law

$$\frac{dp_\phi}{dt} = v_z\frac{dp_\phi}{dz} = qv_z B_r \approx -qv_z\frac{r}{2}\frac{\partial B_z}{\partial z} \tag{11}$$

so that

$$\Delta p_\phi \approx -\frac{qr\Delta B}{2}, \tag{12}$$

where $\Delta B(z = 0) = B_0$ and $\Delta B(z = L) = -B_0$.

An important implication of the model is that the azimuthal kick received by the particle when it enters the solenoid ($z = 0$) cancels that at the exit ($z = L$). This is expected due to conservation of canonical angular momentum [1]. Another important result is that the angle rotated about the axis of the solenoid by the particle's trajectory, ϕ_{lens}, is equal to one-half of the angle rotated about the axis of the helix, ϕ_h as defined in Eq. (8) (see [1]). Hence,

$$\phi_{lens} = \frac{1}{2}\phi_h = -\frac{qB_0 L}{2p}. \tag{13}$$

This can be interpreted as the angle of rotation of a beam when it traverses a solenoid. Note that the angle of rotation is in the $-\hat{\phi}$ direction if the longitudinal velocity v_z is in the same direction of the axial solenoid field B_0 (Lenz's law).

3.2 Particle Tracking

To track a charged particle traveling through a solenoid, we need to know the magnetic field produced by the solenoid. The 3-D magnetic field array can be measured directly, or can be calculated using the measured axial field profile, $B_{z0}(z)$, of the solenoid.

The axial field profile, $B_{z0}(z)$, of the downstream solenoid, SOL-PET, is measured. Using $B_{z0}(z)$, the magnetic field, up to the third order, near the axis of the solenoid can be

calculated as

$$
\begin{aligned}
B_x(x,y,z) &= -\frac{1}{2}xB'_{z0}(z) + \frac{1}{16}x(x^2+y^2)B'''_{z0}(z) - \ldots, \\
B_y(x,y,z) &= -\frac{1}{2}yB'_{z0}(z) + \frac{1}{16}y(x^2+y^2)B'''_{z0}(z) - \ldots, \\
B_z(x,y,z) &= B_{z0}(z) - \frac{1}{4}(x^2+y^2)B''_{z0}(z) + \ldots,
\end{aligned}
\tag{14}
$$

where the "prime" is the derivative with respect to "z".

The motion of a charged particle obeys the Lorentz force law

$$
\frac{d\vec{p}}{dt} = q(\vec{E} + \vec{v} \times \vec{B}). \tag{15}
$$

Assuming change in energy and in the longitudinal velocity v_z of the particle is negligible along the solenoid, we have

$$
\frac{dp_x}{dt} \to \gamma m v_z^2 \frac{d^2x}{dz^2} \qquad \text{and} \qquad \frac{dp_y}{dt} \to \gamma m v_z^2 \frac{d^2y}{dz^2}.
$$

The equations of motion of a particle in a solenoidal field obtained from the Lorentz force law using the above substitution read

$$
\begin{aligned}
x'' &= -\frac{B_y(x,y,z)}{B\rho} + y'\frac{B_z(x,y,z)}{B\rho}, \\
y'' &= \frac{B_x(x,y,z)}{B\rho} - x'\frac{B_z(x,y,z)}{B\rho},
\end{aligned}
\tag{16}
$$

where $B\rho = p/q = \gamma m v/q \approx \gamma m v_z/q$ is the momentum rigidity of the particle.

Using Eq. (14), Eq. (16) and the axial field profile of SOL-PET, protons with a kinetic energy of 48 keV is tracked and its trajectory is plotted in Fig. 6(b). The proton enters the fields at $x(z_i) = 1\,\text{mm}$, $x'(z_i) = 5\,\text{mrad}$, and $y(z_i) = y'(z_i) = 0$. Since the proton enters the fields at zero azimuthal angle on the x-y plane ($\phi = 0$), the proton displaces on the plane an angle

$$
\phi_{track} = \tan^{-1}\left(\frac{y(z_f)}{x(z_f)}\right), \tag{17}
$$

where z_f is the longitudinal location where the solenoid field vanishes. This angle is also the angle of the rotation of a beam when it travels through a solenoid. We note that ϕ_{track} is not sensity to $x'(z_i)$ and $y'(z_i)$ provided that they are $\ll 1$.

3.3 Beam Rotation by SOL-PET

The two focusing solenoids, SOL-U and SOL-PET, are optimized to locate the proton beam waist near the wire scanner to produce decent profile measurement. Beam position is obtained.

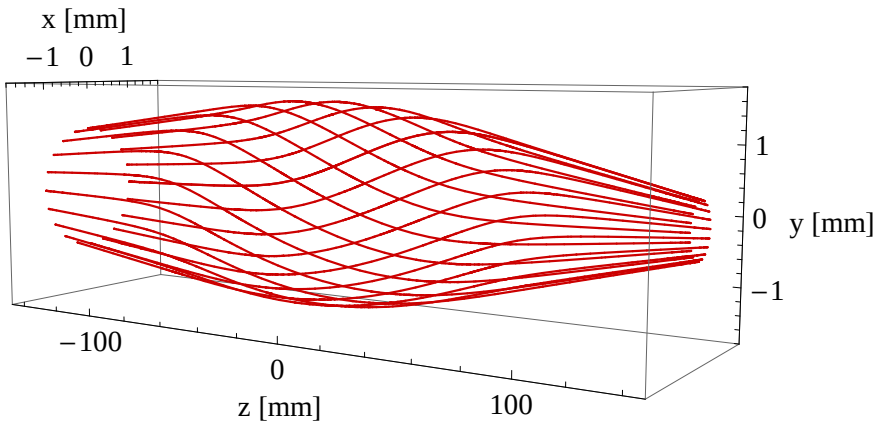

(a) A 3-D plot of the trajectories of 20 protons.

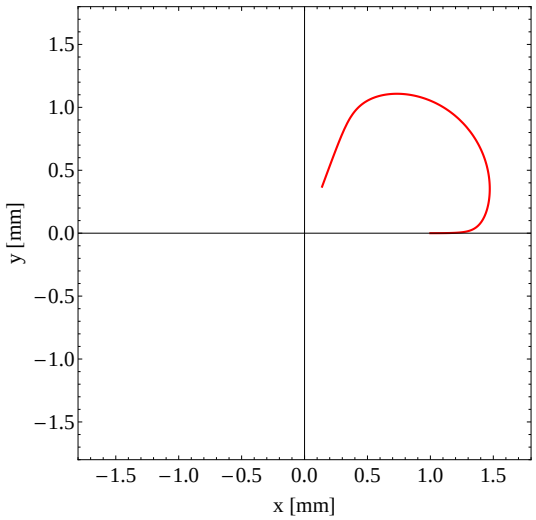

(b) The projection on the $x - y$ plane.

Figure 6: Protons at 48 keV are tracked through the magnetic field produced by SOL-D. (a) The trajectores of 20 protons are simulated. These trajectories represent the beam envelope of a beam. Rotation of the envelope is observed. (b) The proton enters the fields at $x = 1\,\text{mm}$, $x' = 5\,\text{mrad}$, and $y = y' = 0$.

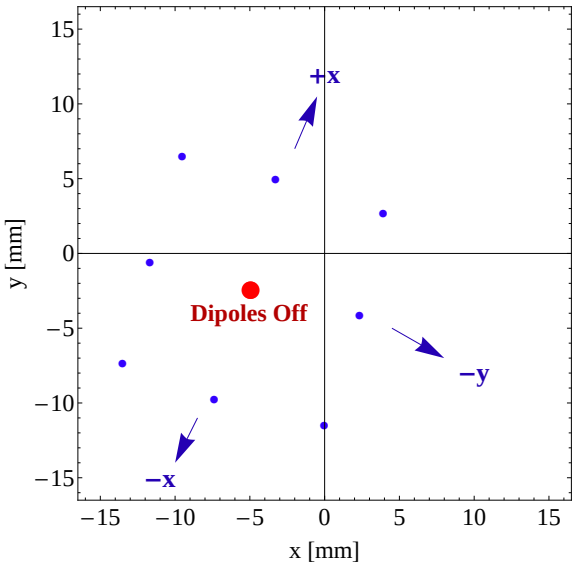

Figure 7: Beam position measurement with different dipole settings. These settings span out a square on the x-y plane. The angle of rotation of the square is the beam rotation due to the solenoid SOL-PET. In this example the beam rotation is +75 degrees.

In the Fig. 7, measurements are made for nine different dipole settings. These settings span out a rotated square on the x-y plane. Since we have shown that there is no x-y coupling when the downstream solenoid is turned off (see Fig. 5), the presence of the solenoid field produced by SOL-PET is the only contribution to the rotation of the square. The angle of rotation of the square is the angle of rotation of the beam. In this example, the beam rotation is $(+75\pm2)$ degrees. The angle of rotation is in the $+\hat{\phi}$ direction because the magnetic field points in the $-\hat{z}$ direction (Len's law).

The angle of beam rotation as a function of solenoid strength is obtained from these measurements and is plotted together with the results from the analyses discussed in Section 3.1 and 3.2. This is shown in Fig. 8. The error for each of the measurements is ±2 degrees. As shown in the figure, three sets of measurement have been made for different SOL-U settings. The amount of beam rotation has no obvious dependence on the strength of SOL-U, as expected. The two approaches discussed in Chapter 3.1 and 3.2 on estimating the amount of beam rotation produce similar results in the region of solenoid strength where the measurement was made. The discrepancy on the two results stems from the fact that ϕ_{lens} calculation is sensitive to the effective length of the solenoid, which is determined by the solenoid field profile measurement. The measurement result is in good agreement with the simulation. Linear fit was performed to data. Result for beam rotation in terms of degree per kGauss is summarized in Table 1.

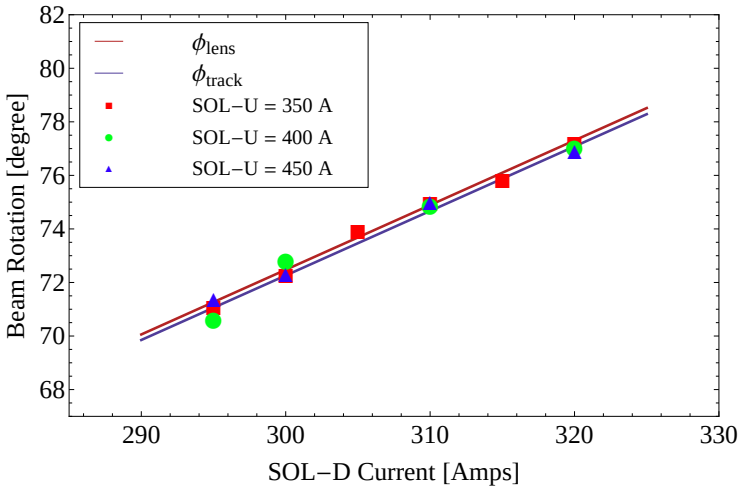

Figure 8: A comparison of the measurement and simulation results for the beam rotation by SOL-PET. The amount of beam rotation has no obvious dependence on the strength of SOL-U, as expected. The two approaches of simulation, ϕ_{lens} and ϕ_{track}, produce similar results. The measurement result is in good agreement with the simulation.

	degrees/Amp	degrees/kGauss
Solenoid Lens	0.242	18.9
Tracking	0.241	18.8
SOL-U 350	0.242	18.9
SOL-U 400	0.245	19.14
SOL-U 450	0.226	17.7

Table 1: Beam rotation per solenoid field − SOL-PET.

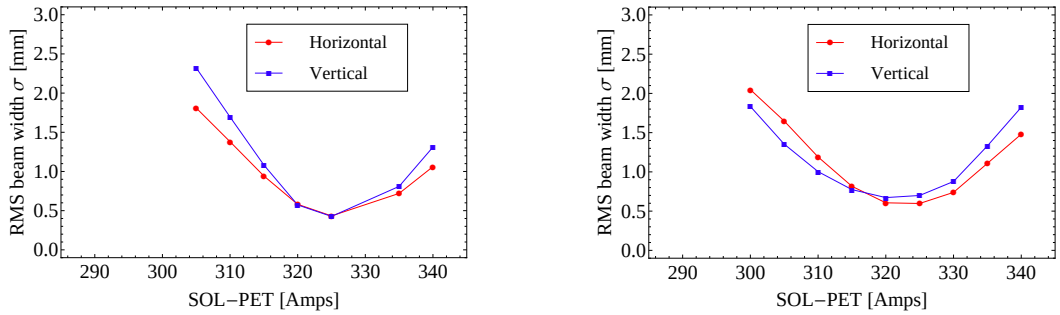

(a) A beam current of 4 mA.

(b) A beam current of 8 mA.

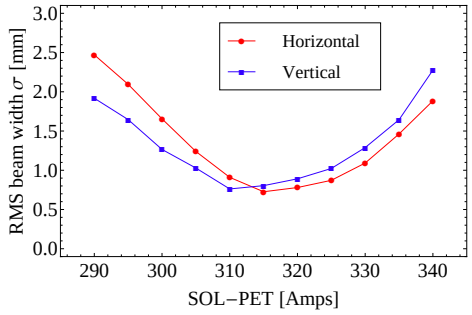

(c) A beam current of 12 mA.

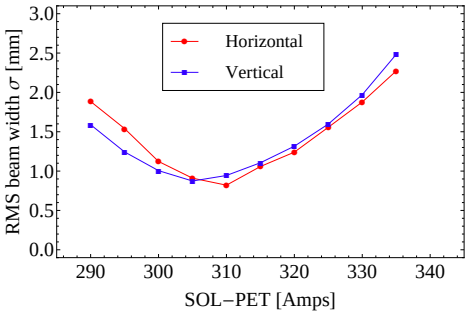

(d) A beam current of 16 mA.

Figure 9: The measured RMS beam width is plotted as a function of the strength of SOL-PET. The two solenoids, SOL-U and SOL-PET, are optimized to locate the beam waist to near the wire scanner. The strength of SOL-U remains unchanged for the measurements.

4 Tranverse Emittance

We have measured emittance using two different methods: solenoid variation method and slit-wire scanner method. Below we dicuss the measurement individually. We then compare the results.

4.1 Measurement using Solenoid Variation Method

The RMS beam size σ changes with the strength of the focusing solenoids. This relation is measured for different beam current and is plotted in Fig. 9. The two solenoids, SOL-U and SOL-PET, are optimized to locate the beam waist to near the wire scanner. The strength of SOL-U remains unchanged for the measurements. Recall from Chapter 1 that the error for these beam width measurements is about $\pm 2\,\%$. These relations can be used to reconstruct the transverse beam emittance. The method is discussed in the following.

Consider the RMS K-V envelope equation:

$$\begin{aligned}\sigma_x'' + k_x(z)\sigma_x - \frac{K_{sc}}{2(\sigma_x+\sigma_y)} - \frac{\epsilon_{x,rms}^2}{\sigma_x^3} = 0,\\ \sigma_y'' + k_y(z)\sigma_y - \frac{K_{sc}}{2(\sigma_x+\sigma_y)} - \frac{\epsilon_{y,rms}^2}{\sigma_y^3} = 0.\end{aligned} \tag{18}$$

where $k_x(z) = k_y(z) = g^2(z) = (\frac{B_z(z)}{2B\rho})^2$ is the solenoid focusing strength, and

$$K_{sc} = \frac{2I_b}{\gamma^3\beta^3 I_0} \tag{19}$$

is the *generalized perveance*. Here I_b is the beam current, γ is the Lorentz factor, $\beta = \sqrt{1-1/\gamma^2}$, and $I_0 = 4\pi\epsilon_0 mc^3/q$ is the characteristic current.

It implies that the analysis is assumed to be in the Larmor rotating frame. The use of decoupled transfer matrix can be justified by the fact that Our 50 keV proton beam is approximately a round beam. So we can decoupled Eq. (18) by setting $\sigma_x = \sigma_y$ and $\epsilon_x = \epsilon_y$. It can be shown that for a round beam with $\sigma_x = \sigma_y$ and $\epsilon_x = \epsilon_y$, under solenoidal focusing channel, beam envelope analysis in the two transverse planes is identical and decoupled, provided that we interpret the results in the Larmor rotating frame. A more detailed discussion on this topic is given in [2].

The solution to Eq. (18), the RMS beam width $\sigma_x(z)$ and $\sigma_y(z)$, can be solved by knowing the Twiss parameter β, α, and the RMS emittance ϵ_{rms}. Fig. 9 shows RMS beam width as a function of solenoid strength. We can used the mentioned three parameters to fit a parabola to the data shown in Fig. 9. RMS beam emittance ϵ_{rms} can then be determined.

The RMS emittance is plotted as a function of the beam current in Fig. 10. Note that the current in the plot is the proton beam current, which is 40% of the total beam current. The major source of uncertainty to this measurement is the drift in SOL-PET excitation current. A drift of 1 Amps in SOL-PET results in up to ± 0.03 mm-mrad or error. Analysis will be given in the next section when we compare the results from the two measurement methods.

4.2 Measurement using Slit-Wire Scanner Method

Another method that has been used for the HINS proton ion source emittance measurement is the slit-wire scanner method. A schemetic drawing of the setup is shown in Fig. 11. The spatial distribution (distribution in x) is scanned by the slit while the angular distribution (distribution in x') is scanned by the wire scanner located a distance L downstream in the beamline. At every position x, the slit is held fixed to allow a portion of the beam to pass through. The particles in the portion (beamlet) reaching to the plane of the wire scanner travel in a straight line [3]. So the angular distribution at every position x of the beam can be measured by the wire scanner, forming density distribution function $\rho(x, x')$ on the $x - x'$ projection of the phase space.

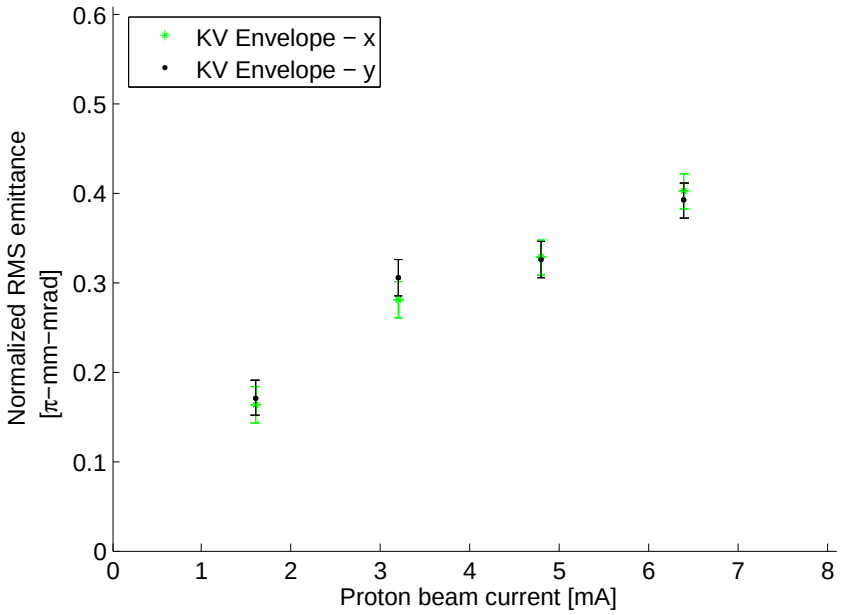

Figure 10: The normalized RMS emittance is plotted as a function of the beam current. The beam current in the plot is the proton current, which is about 40% of the total beam current.

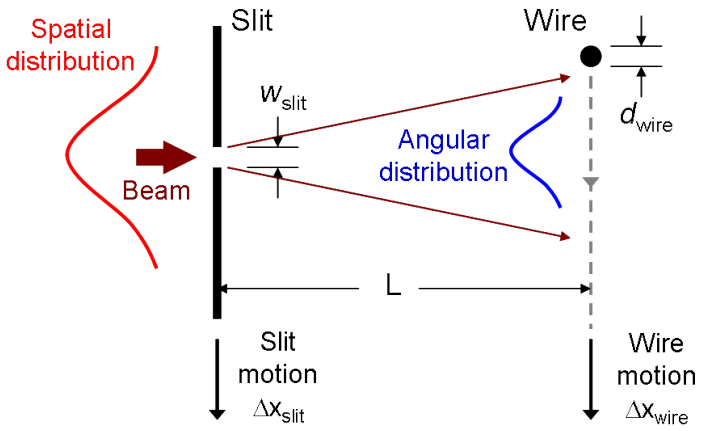

Figure 11: A schemetic drawing of the slit-wire scanner setup.

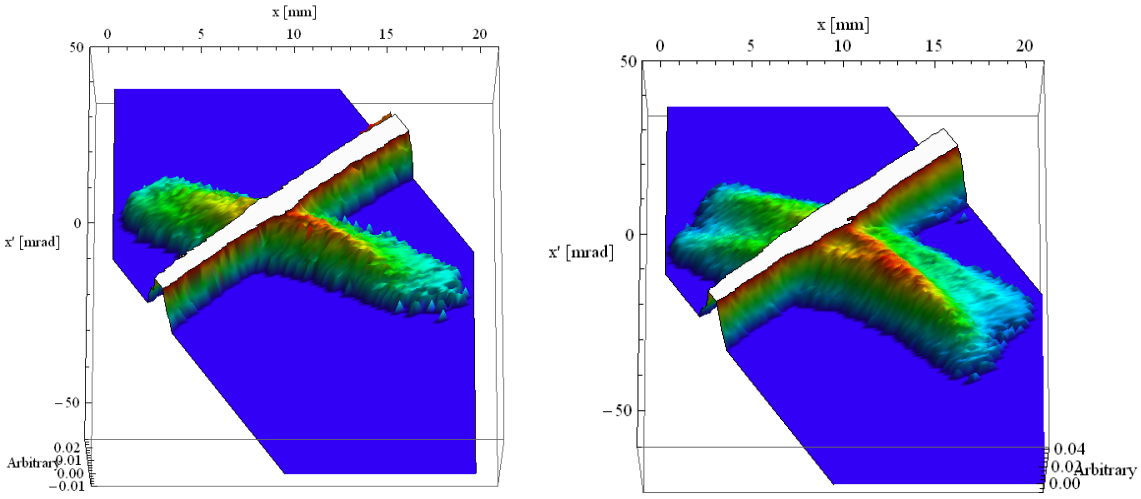

(a) A beam current of 4 mA.

(b) A beam current of 8 mA.

(c) A beam current of 12 mA.

(d) A beam current of 16 mA.

Figure 12: 3D plot of the measured beam distribution $\rho(x, x')$ using the slit-wire scanner assembly. The strip in white is signal from the H_2^+ particle population, which is huge and is out of the plotting range.

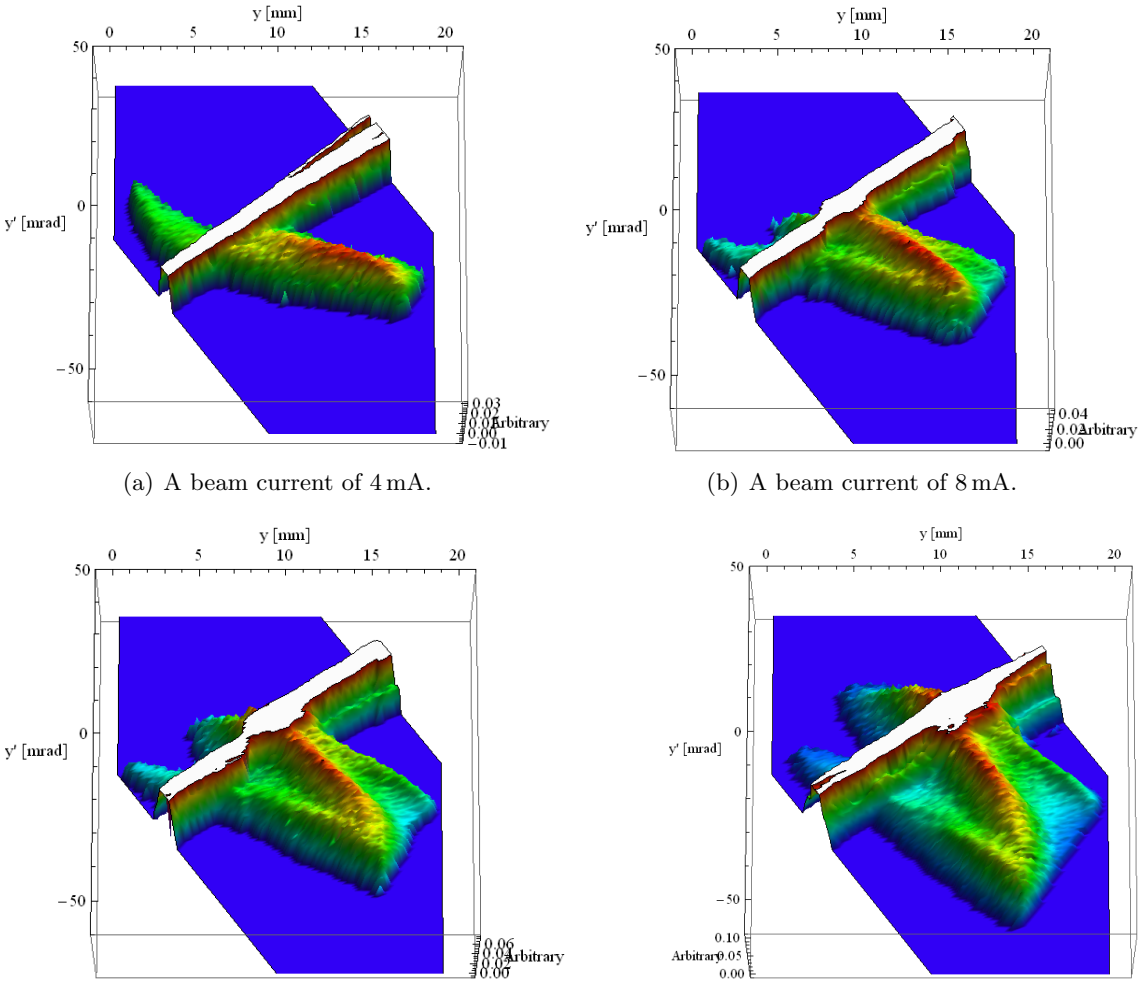

(a) A beam current of 4 mA.

(b) A beam current of 8 mA.

(c) A beam current of 12 mA.

(d) A beam current of 16 mA.

Figure 13: 3D plot of the measured beam distribution $\rho(y, y')$ using the slit-wire scanner assembly. The strip in white is signal from the H_2^+ particle population, which is huge and is out of the plotting range.

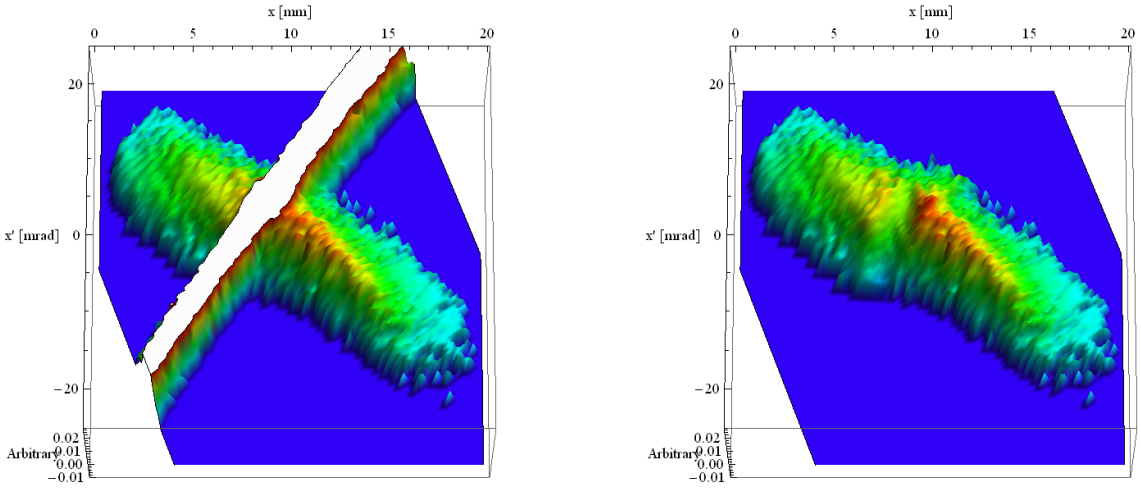

(a) Signal before background subtraction.

(b) Signal with background subtracted.

Figure 14: A comparison of the measurement data before and after background subtraction. Signal near the region of the strip in white is erased. It is then filled up by 2-D interpolation.

The measured density distribution functions in both the $x - x'$ and $y - y'$ phase space planes for different beam current are shown in the 3D density plots in Fig. 12 and 13. In the figures, the island is the signal from the proton while the strip is the signal from the H_2^+ particle population (in white because the signal is huge and is out of the plotting range). As shown in the figures, the beam is convergent at the location of the slit. The beam size is large and the full width of the beam is about 18 mm in both planes for all current. The divergence of the beam increases with the beam current. At larger beam current, the beam appears as an "S" shape in the phase space. This is a sign of non-linearity in focusing/defocusing forces, which includes solenoidal field aberration and space charge force.

To compute the RMS emittance from the measured data, signal from H_2^+ must be subracted. A comparison of the signal before and after background subtraction is shown in Fig. 14. Data near the region of the strip is erased. It is then filled up with 2-D interpolation using the data in the surroundings.

After background subtraction, it is ready to compute the RMS emittance from the data. The cleaned signal is the intensity distribution function $\rho(x_i, x'_j)$. It is a $m \times n$ array storing

the density information. The second moments can be calculated as

$$\langle x^2 \rangle = \frac{\sum_{i=1}^{m} \sum_{j=1}^{n} (x_i - \langle x \rangle)^2 \rho_{ij}}{I_{tot}}, \tag{20}$$

$$\langle x'^2 \rangle = \frac{\sum_{i=1}^{m} \sum_{j=1}^{n} (x'_j - \langle x' \rangle)^2 \rho_{ij}}{I_{tot}}, \tag{21}$$

$$\langle xx' \rangle = \frac{\sum_{i=1}^{m} \sum_{j=1}^{n} (x_i - \langle x \rangle)(x'_j - \langle x' \rangle) \rho_{ij}}{I_{tot}}, \tag{22}$$

where

$$\langle x \rangle = \frac{\sum_{i=1}^{m} \sum_{j=1}^{n} x_i \rho_{ij}}{I_{tot}}, \tag{23}$$

$$\langle x' \rangle = \frac{\sum_{i=1}^{m} \sum_{j=1}^{n} x'_j \rho_{ij}}{I_{tot}}, \tag{24}$$

are the arithmetic mean of the density function $\rho(x_i, x'_j)$. Here $I_{tot} = \sum_{i=1}^{m} \sum_{j=1}^{n} \rho_{ij}$ is the normalization factor. From the second moments, we can construct the RMS emittance

$$\epsilon_{x,rms} = \sqrt{\langle x^2 \rangle \langle x'^2 \rangle - \langle xx' \rangle^2}. \tag{25}$$

The Twiss parameters can also be calculated [4],

$$\begin{aligned} \beta = \frac{\langle x^2 \rangle}{\epsilon_{x,rms}}, \qquad \alpha = -\frac{\langle xx' \rangle}{\epsilon_{x,rms}}, \\ \gamma = \frac{\langle x'^2 \rangle}{\epsilon_{x,rms}} = \frac{1 + \alpha^2}{\beta}. \end{aligned} \tag{26}$$

The cleaned signal is presented as density plot in Fig. 15 and 16. RMS ellipse defined by

$$\epsilon_{x,rms} = \gamma x^2 + 2\alpha xx' + \beta x'^2 \tag{27}$$

is drawn on the top of the phase space density plot.

The RMS emittance as a function of the beam current is compared to the result discussed in Chapter 4.1, where the RMS emittance is deduced from solenoid variation method (Fig. 10). The two sets of results are plotted togehter in Fig. 17. The major source of error for the slit-wire scanner measurement comes from the signal cleaning process. By changing the parameters used in data interpolation, an error of ± 0.05 mm-mrad is recorded.

4.3 Result Analysis

In Fig. 17, results for emittance measurement using two methods, solenoid variation and slit-wire scanner, are compared. We observe that, up to measurement error, the two sets of results agree at lower proton current but diverge at higher current. In this section, we try to explain this observation.

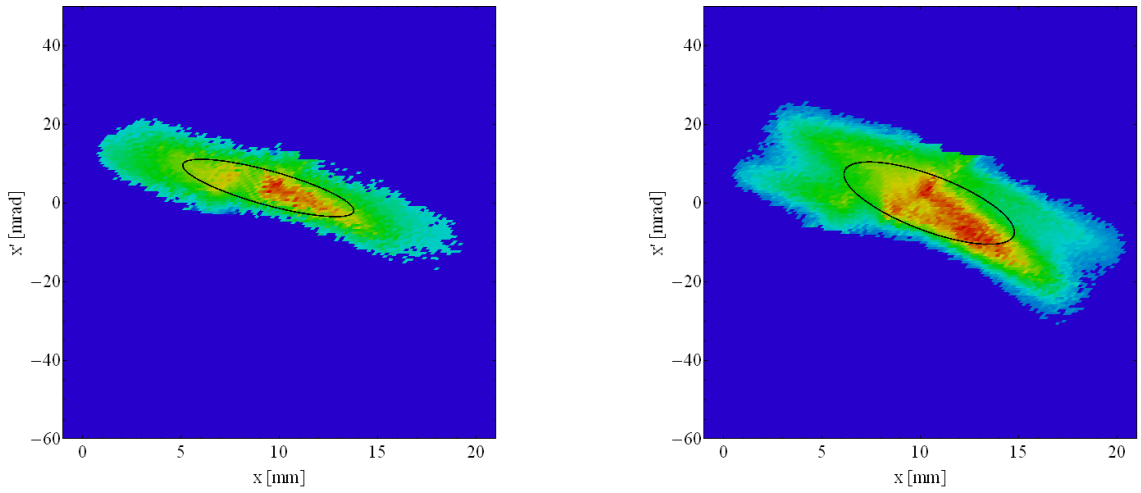

(a) A beam current of 4 mA.

(b) A beam current of 8 mA.

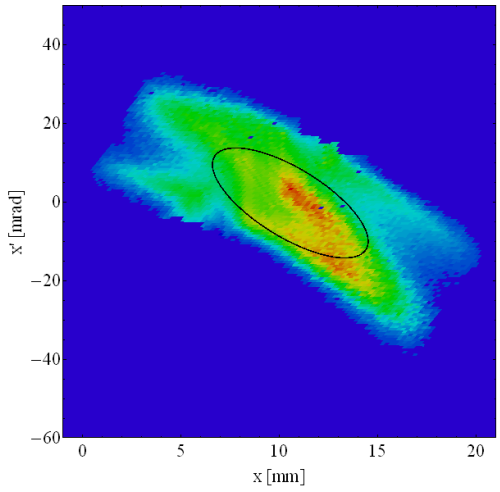

(c) A beam current of 12 mA.

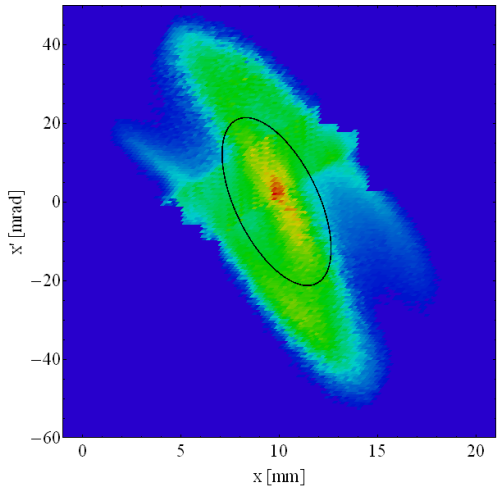

(d) A beam current of 16 mA.

Figure 15: Phase space plot in the $x - x'$ plane. With the cleaned distribution function, the RMS beam emittance and the Twiss parameters can be calculated. Ellipses defined by the Twiss parameters are drawn in the figures.

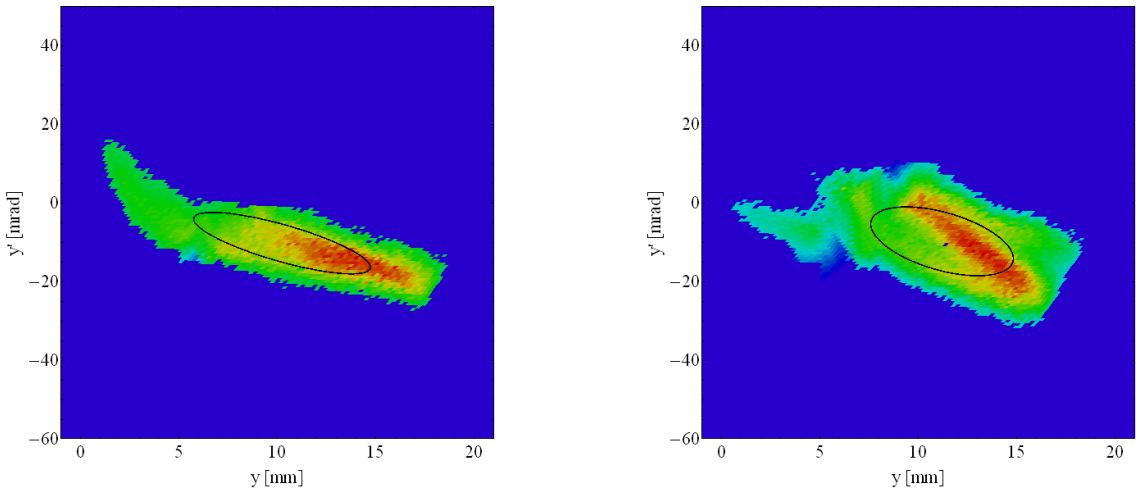

(a) A beam current of 4 mA.

(b) A beam current of 8 mA.

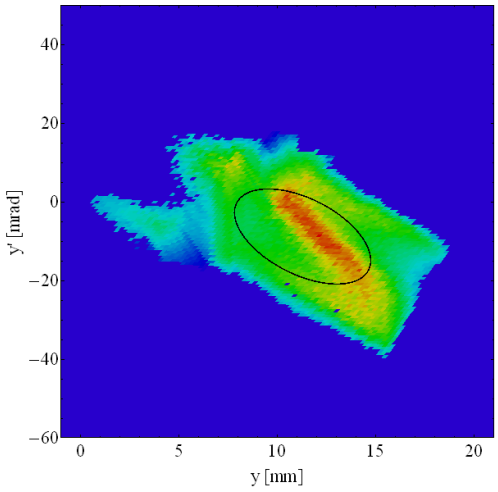

(c) A beam current of 12 mA.

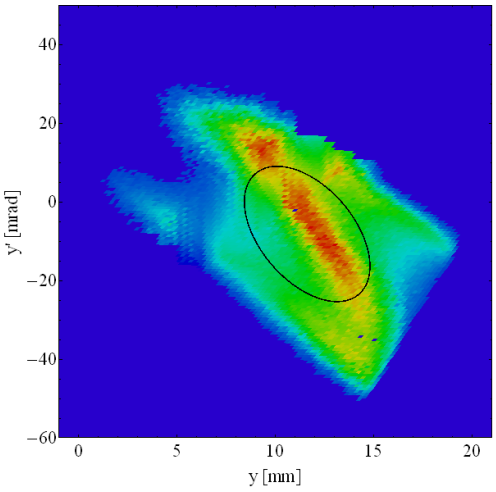

(d) A beam current of 16 mA.

Figure 16: Phase space plot in the $y - y'$ plane. With the cleaned distribution function, the RMS beam emittance and the Twiss parameters can be calculated. Ellipses defined by the Twiss parameters are drawn in the figures.

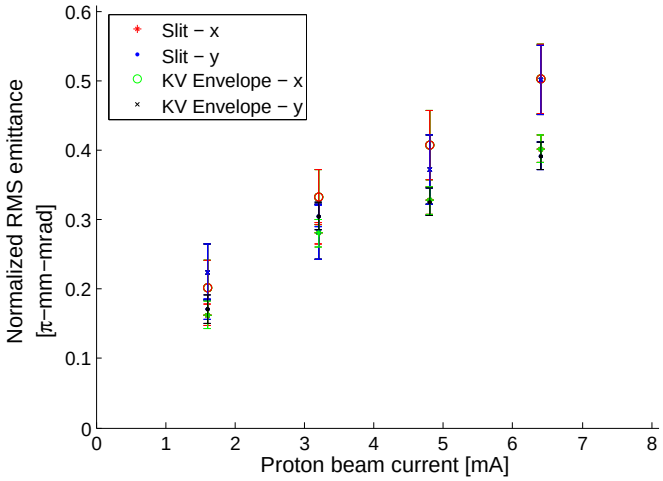

Figure 17: The beam emittance is plotted as a function of the beam current. Results from measurement using the slit-wire scanner assembly and using solenoid variation method are compared.

First of all, it is important to realize that, although we plot them together, the two sets of results describe the beam emittance at two different locations along the beamline. In the solenoid variation method, we used K-V envelope equation to determine the RMS beam emittance at the entrance of the beamline, i.e. the proton ion source. Since space charge effect has been taken into account, the result can be considered as the emittance of the proton source, where space charge does not have enough time to affect the emittance. In the slit-wire scanner method, emittance was measured at the slit-wire scanner assembly, which was the exit of the beamline, which is about 1 m or 320 ns away from the proton source. It is reasonable to interpret the result from the solenoid variation method as the emittance performance of the proton source while the result from the slit method as the effect of space charge on emittance. According to Fig. 17, space charge effect led to emittance growth at higher beam current, which is reasonable.

5 Summary

The HINS proton ion source and low energy beam transport (LEBT) was successfully commissioned. It is capable to produce a 50 keV, 3 msec pulsed beam with a peak current greater than 20 mA (less than 50% proton) at 2.5 Hz (0.7% duty factor).

Beam studies started with interpreting the signal measured by the wire scanner. We successfully extracted the proton signal from a mixture of proton and H_2^+. The have measured the RMS beam width of the proton up to 2% error. Then, we performed a beam-calibration to the steering dipole magnets. The dipole magnets were calibrated and aligned. We then study transverse motion coupling due to solenoidal field by measuring beam rotation through solenoid. Measurement result matches with prediction from beam physics modelings and particle tracking simulations. Finally, transverse beam emittance were measured both directly (slit-wire scanner) and indirectly (solenoid variation). The result from solenoid variation method can be interpret as the emittance performance of the proton source as a function of beam current, since the emittance was determined at the source with space charge effect taken into account. For the slit method, beam emittance was measured at the slit, which is about 1 m or 320 ns away from the source. Space charge effect has enough time to cause emittance growth, which can be observed from the comparison of the two sets of results.

The resutls for our beam studies provide valuable information on the quality of the proton beam. This information is important in beam matching for LEBT to RFQ, beam steering control under solenoidal focusing channel, and etc.

References

[1] K. T. McDonald, "A neutrino horn based on a solenoid lens." `http://puhep1.princeton.edu/~mcdonald/examples/solenoid_lens.pdf`, December 2003.

[2] S. M. Lund and B. Bukh, "Stability properties of the transverse envelope equations describing intense ion beam transport," *PRST-AB*, vol. 7, no. 024801, 2004.

[3] K. T. McDonald and D. P. Russell, *Frontiers of Particle Beams; Observation, Diagnosis and Correction*, vol. 343 of *Lecture Notes in Physics*. Springer Berlin, 1989. p.122-132.

[4] R. Q. Twiss and N. H. Frank *Rev. Sci. Instrum.*, vol. 20, 1949.